Available online at www.sciencedirect.com
SCIENCE DIRECT®
Journal of Sound and Vibration 287 (2005) 129–151
JOURNAL OF SOUND AND VIBRATION
www.elsevier.com/locate/jsvi

Flow-induced cylinder noise formulated as a diffraction problem for low Mach numbers

X. Gloerfelt[a,*], F. Pérot[b], C. Bailly[c], D. Juvé[c]

[a]*Laboratoire de Simulation Numérique en Mécanique des Fluides, ENSAM, 151 boulevard de l'Hôpital, 75013 Paris, France*
[b]*PSA Peugeot Citroën, Centre Technique de Vélizy, 78943 Vélizy Villacoublay, France*
[c]*Laboratoire de Mécanique des Fluides et d'Acoustique, Ecole Centrale de Lyon & UMR CNRS 5509, 69134 Ecully, France*

Received 28 April 2003; received in revised form 25 October 2004; accepted 27 October 2004
Available online 17 February 2005

Abstract

The role of surfaces in the mechanism of sound generation by low Mach number flows interacting with solid nonvibrating surfaces is well established by the classical aeroacoustic papers by Powell, Doak, Ffowcs Williams, Crighton, or Howe. It can be formulated as a problem of diffraction of the flow sources by the rigid body. The present study illustrates this statement in the case of flow-induced cylinder noise. Curle's formulation is analytically and numerically compared to a formulation based on an exact Green's function tailored to a cylindrical geometry. The surface integral of Curle's formulation represents exactly the diffraction effects by the rigid body. The direct and scattered parts of the sound field are studied. In this low Mach number configuration, the cylinder is compact, and the scattered (dipole) field dominates the direct (quadrupole) field. The classical properties of the scattering by a cylinder are retrieved by considering a point quadripole source near the cylinder surface.

*Corresponding author. Tel.: +33 1 44 24 64 31; fax: +33 1 44 24 62 75.
E-mail address: xavier.gloerfelt@paris.ensam.fr (X. Gloerfelt).

0022-460X/$ - see front matter © 2004 Elsevier Ltd. All rights reserved.
doi:10.1016/j.jsv.2004.10.047

1. Introduction

The sound generated by a non-vibrating cylinder in a flow, also known as the æolian tone, is one of the most fundamental aeroacoustic phenomena. The purpose of this paper is to clarify the influence of the cylinder surface in the noise generation mechanism and particularly to point out the role of the diffraction in a low Mach number configuration.

In the most common view, the noise is produced by a fluctuating force exerted by the cylinder on the surrounding fluid, leading to a dipole-like acoustic field. This fluctuating force is associated with the periodic vortex shedding from opposite sides of the cylinder, arranging themselves into a double row called the von Kármán street. This interpretation is closely linked to the formal work of Curle [1] who extended, in 1955, Lighthill's analogy to bounded flows. Curle showed how the role of the surface can be formulated in terms of surface-dipoles and his theory applied successfully to the case of the cylinder flow. In low Mach number compact configurations, i.e. where the size of the body is small compared to the acoustic wavelength, the surface term of Curle's formulation is greater than the volume term. What is the physical role of this surface term? The interpretation of Yudin [2], Curle [1], Phillips [3], Goldstein [4], or Blake [5], relating the noise to the fluctuating aerodynamic force on the obstacle, is not clear considering Powell's remark [6]: *the fluctuating force itself*, *in the real situations*, *cannot possibly generate acoustic energy*, *since it acts at a rigid surface*. So the aforementioned force is only of the nature of an equivalent source, and the acoustic energy should rather come from the unsteady flow itself.

The origin of this acoustic energy has been studied by Doak [17], Ffowcs Williams [7], Ffowcs Williams and Hall [8], Crighton and Leppington [9], Crighton [10], who clearly identified the diffraction of the volume-sources radiation as a very efficient phenomenon in compact cases. Considering the case of the cylinder at low Mach number, Powell [6], Howe [11], Dowling [12], or Hardin and Lamkin [13] have recovered the dipolar character of the cylinder noise using formulations based on the vortical fluctuations in the flow, with no use of the surface pressure fluctuations.

In the present paper, the mechanism of diffraction by the cylinder is illustrated. The analytical expressions of Lighthill's analogy first in the Curle form (free-field Green function), then based on a tailored Green's function, verifying the rigidity condition on the cylinder $\partial G/\partial n = 0$, are derived in Section 2. A numerical illustration is then presented in Section 3. A two-dimensional (2-D) incompressible RANS (Reynolds Averaged Navier–Stokes) aerodynamic simulation is performed to provide both the T_{ij} and the pressure distribution p at the cylinder surface. The results obtained with Curle's formulation and the formulation based on the tailored Green function are compared. In Section 4, the sound radiated by a point quadrupole source near the cylinder illustrates the mechanism by which the noise is enhanced. This analysis is quite similar to that of Davies [14] for the case of a rigid sphere. In particular, the dipole-like radiation is recovered both numerically and analytically.

2. Analytical formulae

In this section, the equivalence between the surface integral of Curle's formulation and the diffraction of the volume sources by the cylinder is derived in the 2-D frequency-domain, by taking the Green formula as a common starting point.

2.1. The acoustic analogy

The aim is to predict the acoustic field radiated by an unsteady flow confined to a bounded region. An acoustic analogy for this problem consists of a forced wave equation:

$$\left(\nabla^2 - \frac{1}{c_\infty^2}\frac{\partial^2}{\partial t^2}\right)\phi(\mathbf{x},t) = q(\mathbf{x},t), \tag{1}$$

where c_∞ is the sound speed, and ϕ a field variable which can be the pressure or density perturbation in the acoustic region. The source q can be estimated independently from a knowledge of the unsteady flow. Many choices are possible for the expression of q [15], and Lighthill's analogy [16] is followed here. The inhomogeneous wave equation for the density is obtained by an exact recombination of the continuity and momentum equations, yielding to:

$$q = -\frac{1}{c_\infty^2}\frac{\partial^2 T_{ij}}{\partial x_i \partial x_j}, \quad \text{in which } T_{ij} = \rho u_i u_j + P_{ij} - c_\infty^2 \rho \delta_{ij} \tag{2}$$

defines Lighthill's tensor in terms of velocity components u_i, compressive stress tensor P_{ij}, and density ρ. $P_{ij} = p\delta_{ij}$ if viscous terms are neglected.

The 2-D formulations are written in the frequency domain by using the Fourier transform, defined as

$$\hat{\phi}(\mathbf{x},\omega) = \int_{-\infty}^{\infty} \phi(\mathbf{x},t)\mathrm{e}^{\mathrm{i}\omega t}\,\mathrm{d}t. \tag{3}$$

This choice makes easier the derivations in cylindrical coordinates, and avoids the time integration by solving the problem harmonically. This is convenient for 2-D applications, where no simple retarded time solution is available. Moreover, this approach avoids numerical differentiations of flow quantities, and accordingly increases the accuracy of the results. Its use is well-justified for the 2-D cylinder flow, characterized by a pseudoperiodic vortex shedding.

2.2. Formulations in presence of surfaces

2.2.1. Green's formula

In a first step, the problem of determining the field $\hat{\phi}$ at an observer point $\mathbf{x}$ in a finite volume V bounded by a surface Σ is considered. Inside V, the field $\hat{\phi}$ satisfies the inhomogeneous Helmholtz equation:

$$(\nabla^2 + k^2)\hat{\phi}(\mathbf{x},\omega) = \hat{q}(\mathbf{x},\omega), \tag{4}$$

where $k = \omega/c_\infty$ is the wavenumber, and $\hat{q}$ is the source field. The surface Σ is defined by the equation $f = 0$: f is such that $f > 0$ inside V and $f < 0$ outside. Eq. (4) is multiplied by the Heaviside function $H(f)$ to obtain a form valid over all space, and the wave equation for $H\hat{\phi}$ is formed:

$$(\nabla^2 + k^2)(H\hat{\phi}) = H\hat{q} + \nabla H \cdot \nabla\hat{\phi} + \nabla\cdot(\hat{\phi}\nabla H). \tag{5}$$

An integral solution is generated by convoluting Eq. (5) with the Green function $\hat{G}$ satisfying the equation:

$$(\nabla^2 + k^2)\hat{G}(\mathbf{x}|\mathbf{y},\omega) = \delta(\mathbf{x}-\mathbf{y}) \tag{6}$$

representing the response in $\mathbf{x}$ due to a point source in $\mathbf{y}$. The Green function is not uniquely defined by Eq. (6); any solution of the homogeneous problem can be added. The convolution product yields:

$$H(f)\hat{\phi}(\mathbf{x},\omega) = \iint_{-\infty}^{\infty} H(f)\hat{q}(\mathbf{y},\omega)\hat{G}(\mathbf{x}|\mathbf{y},\omega)\,\mathrm{d}\mathbf{y} + \iint_{-\infty}^{\infty} \hat{G}(\mathbf{x}|\mathbf{y},\omega)\{\nabla H\cdot\nabla\hat{\phi} + \nabla\cdot(\hat{\phi}\nabla H)\}\,\mathrm{d}\mathbf{y}.$$

The Heaviside function reduces the first integral on the volume (surface in 2-D) V ($f>0$). The second one is modified by including $\hat{G}$ inside the gradient operators, integrating by parts, and using the relation $\nabla H = \nabla f\,\delta(f)$:

$$H(f)\hat{\phi}(\mathbf{x},\omega) = \iint_{V(\mathbf{y})} \hat{q}(\mathbf{y},\omega)\hat{G}(\mathbf{x}|\mathbf{y},\omega)\,\mathrm{d}\mathbf{y} + \iint_{-\infty}^{\infty}\left\{\hat{G}\,\frac{\partial\hat{\phi}}{\partial y_i} - \hat{\phi}\,\frac{\partial\hat{G}}{\partial y_i}\right\}\frac{\partial f}{\partial y_i}\,\delta(f)\,\mathrm{d}\mathbf{y}.$$

The function f is scaled so that $\nabla f/|\nabla f|$ is the surface normal $\mathbf{n}$, pointing inside V ($f>0$). By using Green's theorem, the second integral is evaluated on the surface (line in 2-D) Σ:

$$H(f)\hat{\phi}(\mathbf{x},\omega) = \iint_{V} \hat{q}(\mathbf{y},\omega)\hat{G}(\mathbf{x}|\mathbf{y},\omega)\,\mathrm{d}\mathbf{y} + \int_{\Sigma}\left\{\hat{G}\,\frac{\partial\hat{\phi}}{\partial y_i} - \hat{\phi}\,\frac{\partial\hat{G}}{\partial y_i}\right\}n_i\,\mathrm{d}\Sigma(\mathbf{y}). \tag{7}$$

This is the *Green formula* in the frequency domain, which can be solved with any desired Green function.

2.2.2. Formulation A: Curle's analogy

Curle's method [1] consists in using the free-field Green function $\hat{G}_0$ in the Green formula, written for the density.

$$H(f)\hat{\rho}(\mathbf{x},\omega) = -\frac{1}{c_\infty^2}\iint_{V}\frac{\partial^2\hat{T}_{ij}}{\partial y_i\partial y_j}\,\hat{G}_0\,\mathrm{d}\mathbf{y} + \int_{\Sigma}\left\{\hat{G}_0\,\frac{\partial\hat{\rho}}{\partial y_i} - \hat{\rho}\,\frac{\partial\hat{G}_0}{\partial y_i}\right\}n_i\,\mathrm{d}\Sigma(\mathbf{y}).$$

The differentiations in the volume integral are transferred on $\hat{G}_0$ by applying integration by parts twice:

$$H(f)c_\infty^2\hat{\rho}(\mathbf{x},\omega) = -\iint_{V}\hat{T}_{ij}\,\frac{\partial^2\hat{G}_0}{\partial y_i\partial y_j}\,\mathrm{d}\mathbf{y} + \int_{\Sigma}\left\{\hat{G}_0\,\frac{\partial\hat{T}_{ij}}{\partial y_j}\,n_i - \hat{T}_{ij}\,\frac{\partial\hat{G}_0}{\partial y_i}\,n_j\right\}\mathrm{d}\Sigma(\mathbf{y}) + c_\infty^2\int_{\Sigma}\left\{\hat{G}_0\,\frac{\partial\hat{\rho}}{\partial y_i} - \hat{\rho}\,\frac{\partial\hat{G}_0}{\partial y_i}\right\}n_i\,\mathrm{d}\Sigma(\mathbf{y}).$$

Using the definition of $\hat{T}_{ij}$, and its symmetry property, it yields:

$$H(f)\hat{p}(\mathbf{x},\omega) = -\iint_V \hat{T}_{ij}\frac{\partial^2\hat{G}_0}{\partial y_i\partial y_j}\,\mathrm{d}\mathbf{y} + \int_\Sigma \hat{G}_0\frac{\partial(\widehat{\rho u_i u_j}+\hat{P}_{ij})}{\partial y_i}\,n_i\,\mathrm{d}\Sigma(\mathbf{y}) - \int_\Sigma (\widehat{\rho u_i u_j}+\hat{P}_{ij})\frac{\partial\hat{G}_0}{\partial y_j}\,n_i\,\mathrm{d}\Sigma(\mathbf{y}).$$

The previous expression is simplified in the case of a rigid surface, where $\partial\hat{p}/\partial n = 0$, the viscous terms are neglected, and the no-slip condition $\hat{u}_i = 0$ applies:

$$H(f)\hat{p}(\mathbf{x},\omega) = -\iint_V \hat{T}_{ij}\frac{\partial^2\hat{G}_0}{\partial y_i\partial y_j}\,\mathrm{d}\mathbf{y} - \int_\Sigma \hat{p}\frac{\partial\hat{G}_0}{\partial y_i}\,n_i\,\mathrm{d}\Sigma(\mathbf{y}), \tag{8}$$

which is Curle's extension of Lighthill's analogy for a rigid body in a medium at rest.

2.2.3. Formulation B: Tailored Green's function

An alternative to solve Green's formula (7) is to consider a tailored Green's function, which satisfies a prescribed boundary condition on Σ. Eq. (8) for a tailored Green's function $\hat{G}_1$ is

$$H(f)\hat{p}(\mathbf{x},\omega) = -\iint_V \hat{T}_{ij}\frac{\partial^2\hat{G}_1}{\partial y_i\partial y_j}\,\mathrm{d}\mathbf{y} - \int_\Sigma \hat{p}\frac{\partial\hat{G}_1}{\partial y_i}n_i\,\mathrm{d}\Sigma(\mathbf{y}).$$

For a hard surface, $\hat{G}_1$ is determined such that $\partial\hat{G}_1/\partial n = 0$ on Σ. The entire surface (line in 2-D) term vanishes to leave the solution as a volume (surface in 2-D) integral:

$$H(f)\hat{p}(\mathbf{x},\omega) = -\iint_V \hat{T}_{ij}\frac{\partial^2\hat{G}_1}{\partial y_i\partial y_j}\,\mathrm{d}\mathbf{y}. \tag{9}$$

The difficulty is now transferred on the construction of a tailored Green function $\hat{G}_1$. Comparing formulations (8) and (9), it yields:

$$\int_\Sigma \hat{p}\frac{\partial\hat{G}_0}{\partial y_i}\,n_i\,\mathrm{d}\Sigma(\mathbf{y}) = \iint_V \hat{T}_{ij}\frac{\partial^2\hat{G}_s}{\partial y_i\partial y_j}\,\mathrm{d}\mathbf{y}, \tag{10}$$

where $\hat{G}_s$ is the part of $\hat{G}_1$ representing the presence of the cylinder. Thus, the surface (line in 2-D) integral in the Curle analogy represents the scattering of the aerodynamic source by the cylinder, as discussed for instance by Doak [17].

2.3. Two-dimensional free-field Green's function in frequency-domain

2.3.1. Rectangular coordinate system

With the conventions for the Fourier transform (3), the 2-D free-field Green function of Eq. (6) is

$$\hat{G}_0(\mathbf{x}|\mathbf{y},\omega) = \frac{1}{4\mathrm{i}}H_0^{(1)}(kr) \quad \text{with } r = \sqrt{(x_1-y_1)^2+(x_2-y_2)^2}, \tag{11}$$

where $H_0^{(1)}$ is the Hankel function of the first kind of order zero. (x_1,x_2) and (y_1,y_2) are the components of $\mathbf{x}$ and $\mathbf{y}$ in the rectangular coordinate system, as sketched in Fig. 1.

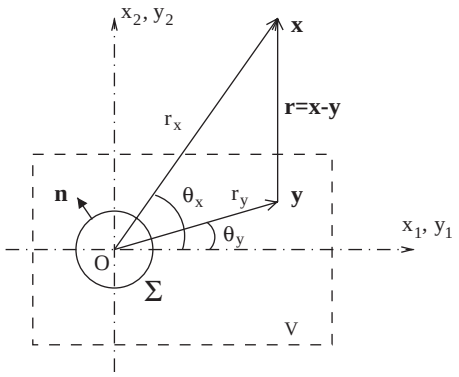

Fig. 1. Notations and coordinate systems used for the acoustic formulations.

2.3.2. Cylindrical coordinate system

The previous Green function can also be expressed in cylindrical coordinates, $\mathbf{x} = (r_x, \theta_x)$ and $\mathbf{y} = (r_y, \theta_y)$. The expansion is given by Morse and Ingard [18]:

$$\hat{G}_0(\mathbf{x}|\mathbf{y}, \omega) = \frac{1}{4\mathrm{i}} \sum_{m=0}^{+\infty} \varepsilon_m \cos m(\theta_y - \theta_x) \times \begin{cases} H_m^{(1)}(kr_x) J_m(kr_y), & r_y \leqslant r_x, \\ J_m(kr_x) H_m^{(1)}(kr_y), & r_y \geqslant r_x, \end{cases} \tag{12}$$

where $\varepsilon_m = 1$ for $m = 0$ and $\varepsilon_m = 2$ for $m > 0$, J_m is the Bessel function of mth order, and $H_m^{(1)}$ is the mth order Hankel function of the first kind.

2.4. Scattering from a cylinder

The problem of scattering from a cylinder of radius a is now considered. The total pressure $\hat{p}$ is usually split into the undisturbed pressure $\hat{p}_0$, which would be present if the cylinder were not there, and the scattered pressure $\hat{p}_s$, as

$$\hat{p} = \hat{p}_0 + \hat{p}_s. \tag{13}$$

The source field of amplitude A is expressed in terms of cylindrical waves as

$$\hat{p}_0 = \frac{A}{4\mathrm{i}} \sum_{m=0}^{+\infty} \varepsilon_m \cos m(\theta_y - \theta_x) H_m^{(1)}(kr_x) J_m(kr_y). \tag{14}$$

When the cylinder is present, it distorts this incident wave, and, in addition to the source field, there is a scattered outgoing wave of such size and shape as to make the normal pressure gradient of the combination zero at $r_y = a$. If the form of this outgoing wave is chosen to be the infinite sum:

$$\hat{p}_s(\mathbf{x}, \omega) = \sum_{m=0}^{+\infty} \varepsilon_m A_m H_m^{(1)}(kr_y) \cos m(\theta_y - \theta_x),$$

the condition $\partial\hat{p}/\partial r_y = 0$ at $r_y = a$ yields:

$$A_m = -\frac{A}{4\mathrm{i}} \frac{J_{m-1}(ka) - J_{m+1}(ka)}{H_{m-1}^{(1)}(ka) - H_{m+1}^{(1)}(ka)} H_m^{(1)}(kr_x).$$

The scattered pressure is then:

$$\hat{p}_s = -\frac{A}{4\mathrm{i}} \sum_{m=0}^{+\infty} \varepsilon_m \cos m(\theta_y - \theta_x) \times \frac{J_{m-1}(ka) - J_{m+1}(ka)}{H^{(1)}_{m-1}(ka) - H^{(1)}_{m+1}(ka)} H^{(1)}_m(kr_x) H^{(1)}_m(kr_y). \tag{15}$$

A particular form of the result given by Morris [19] for the diffraction of a cylindrical line source by a cylinder is recovered for the case of a rigid cylinder.

2.5. Construction of a tailored Green function

The use of an exact Green's function tailored to body geometry has the nice feature of a simple integral equation (9), and is well-suited to simple geometries. The first application was in 1960 by Powell [20], or Doak [17], to the case of an infinite plane boundary. Ffowcs Williams and Hall [8] and Jones [21] treated the case of a sharp-edged large surface. Davies [14] considered the case of a rigid sphere. This case is also studied by Crighton and Leppington [9] together with the semi-infinite plane and the wedge problems. This kind of approaches is generalized with the introduction of compact Green's function [22] in the vortex sound theory. For the case of cylinder flow, Powell [6] recovered the dipole character of the sound field by using the images of the periodically shed vortices by the cylinder surface. Hardin and Lamkin [13] and Howe [11] applied the vortex sound theory to the æolian tone by considering the appropriate compact Green function. Dowling [12] also applied this formalism by using a vector Green's function in Möhring's formulation.

In general, the construction of the tailored Green function is equivalent to considering the acoustic response of the body. In the present study, to obtain a tailored Green's function, any solution of the homogeneous Helmholtz equation can be added to the free-field Green function. This additional term can serve to fit the boundary condition at the surface of the cylinder. Following the previous section, the additional Green function is made up of Hankel functions of the first kind, which represent waves going outward:

$$\hat{G}_s(r_x, \theta_x | r_y, \theta_y, \omega) = \frac{1}{4\mathrm{i}} \sum_{m=0}^{+\infty} \varepsilon_m B_m H^{(1)}_m(kr_y) \cos m(\theta_y - \theta_x). \tag{16}$$

The term $\hat{G}_s$ is a solution of the homogeneous Helmholtz equation, and $\hat{G}_1 = \hat{G}_0 + \hat{G}_s$ is also a Green's function for Eq. (6). As previously, the condition $\partial \hat{G}_1 / \partial r_y = 0$ at $r_y = a$ yields:

$$B_m = -\frac{J_{m-1}(ka) - J_{m+1}(ka)}{H^{(1)}_{m-1}(ka) - H^{(1)}_{m+1}(ka)} H^{(1)}_m(kr_x),$$

$\hat{G}_s$ is caused by the presence of the cylinder, and is thus termed the scattered part of the tailored Green's function, written as

$$\hat{G}_s = -\frac{1}{4\mathrm{i}} \sum_{m=0}^{+\infty} \varepsilon_m \cos m(\theta_y - \theta_x) \times \frac{J_{m-1}(ka) - J_{m+1}(ka)}{H^{(1)}_{m-1}(ka) - H^{(1)}_{m+1}(ka)} H^{(1)}_m(kr_x) H^{(1)}_m(kr_y) \tag{17}$$

and the tailored Green $\hat{G}_1$ function reads:

$$\hat{G}_1(\mathbf{x}|\mathbf{y},\omega) = \frac{1}{4\mathrm{i}} \sum_{m=0}^{+\infty} \varepsilon_m \cos m(\theta_y - \theta_x) \left[H_m^{(1)}(kr_x) J_m(kr_y) - \frac{J_{m-1}(ka) - J_{m+1}(ka)}{H_{m-1}^{(1)}(ka) - H_{m+1}^{(1)}(ka)} H_m^{(1)}(kr_x) H_m^{(1)}(kr_y) \right]. \quad (18)$$

A similar expression is obtained by Davies [14] for a rigid sphere.

3. Numerical illustration

3.1. Aerodynamic simulation

3.1.1. Configuration and numerical method

The 3-D simulations of cylinder flow for high Reynolds numbers are still hardly achievable because the meshgrid should resolve precisely the transition of the boundary layers on the cylinder surface. To obtain a sufficiently representative flow at $Re_D \sim 10^5$, a 2-D circular cylinder is simulated by solving the incompressible unsteady Reynolds Averaged Navier–Stokes (U-RANS) equations. Even if the flow behind a cylinder is 3-D for $Re_D \gtrsim 200$, the 2-D approach can give an acceptable representation of the flow-field, dominated by alternately and periodically vortex shedding from opposite sides of the cylinder.

Moreover, since the analytical formulae (8) and (9) are 2-D, the choice of a 2-D approach is convenient and allows to keep tractable simulation times and database sizes. This incompressible flow solution will provide the aerodynamic sources, namely the quadrupoles T_{ij} and the pressure at the cylinder surface.

The cylinder diameter D is 3.81 cm (1.5 in), and the Mach number of the uniform flow in x_1 direction is $M = 0.12$, corresponding to a Reynolds number $Re_D \simeq 1.1 \times 10^5$. A U-RANS simulation using the Reynolds Stress Model was performed with the FLUENT CFD code on an unstructured meshgrid of about 55,000 points. The computational domain extends from $-8.5D$ to $16.5D$ in the streamwise direction, and from $-10.5D$ and $10.5D$ vertically. The two-layer method is used near the cylinder wall. In the inner layer, the boundary layer equation is integrated to the wall, so that grids with minimum spacings on the order of $\Delta y^+ \simeq 1$ must be employed to ensure adequate resolution. The cylinder surface is discretized with 350 points giving values of Δy^+ between 0.3 and 1.1 on the cylinder circumference. The initial free-stream turbulent level is around 1%; the time step is $\Delta t = 10^{-4}$ s, yielding to about $35\Delta t$ per shedding cycle.

3.1.2. Validation of aerodynamic results

When $Re_D > 47$, vortices are shed alternately and periodically from opposite sides of the cylinder. It is the onset of the von Kármán vortex street. The increase in Reynolds number is accompanied with various regimes, resulting from the successive transition of the wake, the shear layers, and the boundary layers on the cylinder [23]. In the present simulation, the chosen Reynolds number of 1.1×10^5 is located in the transition regime of the boundary layer, which is very sensitive to small

disturbances, such as free-stream turbulence and surface roughness [24,25]. The onset of this critical region can vary between 10^5 and 5×10^5, depending on the special flow conditions.

For the present simulation, the simple eddy viscosity model used for the turbulent closure is not able to describe a transitional state, and the boundary layers around the cylinder are considered fully turbulent. The direct consequence is the position of the separation point located near an angle of $\theta = 110^\circ$ instead of $\theta = 80^\circ$. This angle corresponds to a more turbulent flow. The wake is then narrower, and the mean drag coefficient is reduced to $\overline{C}_D = 0.47$. Consequently, the Strouhal number of the global von Kármán mode is increased to $St = f_0 D/U_\infty = 0.24$. The equivalent Reynolds number would be that of a transcritical regime, as described by Roshko [26] for Reynolds numbers of roughly 4 million.

Fig. 2(a) shows the mean pressure coefficient C_p distribution on the cylinder. Its shape agrees well with the measurements of Batham [24] for the same Reynolds number but with a high-level of incoming turbulence (grid turbulence). For comparison, the results of Batham for a uniform stream across the cylinder is also plotted, and shows the expected behaviour for a subcritical flow, as reported by Revell et al. [27] ($Re_D = 9 \times 10^4$), Achenbach [28] ($Re_D = 10^5$), or Cantwell and Coles [29] ($Re_D = 1.4 \times 10^5$). The mean drag coefficient is 1.17 for the configuration of Batham with a uniform incoming stream, and drops to 0.41 in the turbulent flow.

Fig. 2(b) shows portions of the time histories of the drag and lift coefficient, noted respectively C_D and C_L. The lift coefficient varies with a Strouhal number of 0.24. The drag is also pseudo-periodic with twice the frequency of the lift. It is however modulated by the frequency of the shedding cycle, indicating a slight asymmetry of the flow.

he coherent structures are plotted in Fig. 3, showing the alternate vortex shedding from upper and lower edge of the cylinder, and their appearance about $x_1/D \simeq 1.5$, behind the cylinder. Averaged Reynolds stresses are shown in Fig. 4. Both components reach their maximum values near the end of the vortex-formation region, defining the *formation length*, $L_f \simeq 1.5D$. Their global shape is similar to the corresponding experimental contours of the Reynolds stresses for the periodic part of the motion at $Re_D = 1.4 \times 10^5$, reported by Cantwell and Coles [29]. The levels of turbulent intensities are also in reasonably good agreement. The highest experimental contours

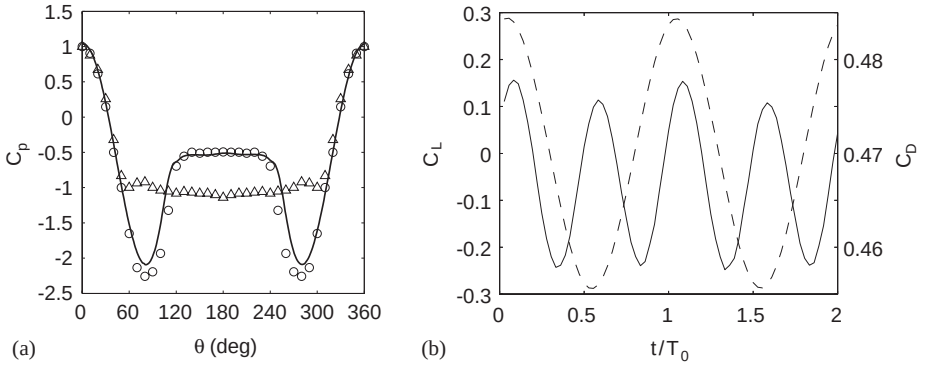

Fig. 2. (a) Distribution of mean pressure coefficient around the cylinder: (——), present simulation at $Re_D = 1.1 \times 10^5$; symbols, experimental data at $Re_D = 1.11 \times 10^5$, from Batham [24], (○ ○ ○), smooth cylinder in turbulent stream, and (△ △ △), smooth cylinder in uniform stream. (b) Time histories of the adimensionalized surface pressure forces: (——) drag coefficient defined as $C_D = \int_0^{2\pi} p \cos\theta \, d\theta/\rho_\infty U_\infty^2$; (– – –) lift coefficient, $C_L = \int_0^{2\pi} p \sin\theta \, d\theta/\rho_\infty U_\infty^2$.

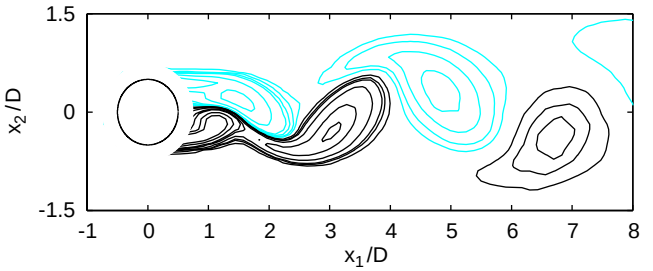

Fig. 3. Vorticity snapshot. 16 contours between $\Omega D/U_\infty = -4.43$ and 4.43: (——) negative contours, (——) positive contours. Zoom around the cylinder wake.

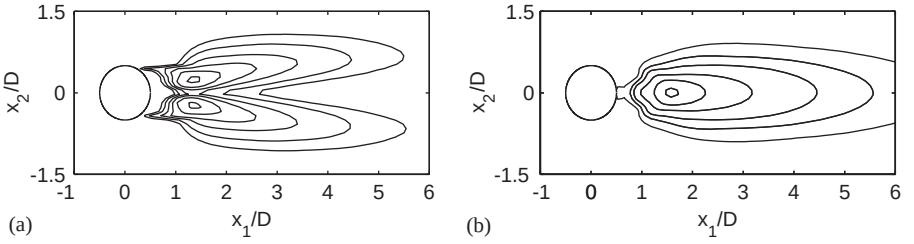

Fig. 4. (a) Contours for mean streamwise Reynolds stress $u_{1_{\rm rms}}/U_\infty$ (isocontour values: 0.1, 0.15, 0.2, 0.3, 0.4). (b) Contours for mean crossflow Reynolds stress $u_{2_{\rm rms}}/U_\infty$ (isocontour values: 0.1, 0.2, 0.3, 0.4, 0.48).

are 0.28 and 0.48 for the streamwise and crossflow components. The predicted levels are $u_{1_{\rm rms}}/U_\infty \simeq 0.4$, and $u_{2_{\rm rms}}/U_\infty \simeq 0.48$.

To summarize, the characteristics of the simulation correspond to a transcritical flow because of the forced turbulent state of the boundary layer. This trend has been identified in previous numerical studies [30,31]. Even oversimplified by the 2-D approach, a coherent aerodynamic field including the structures responsible for the æolian tone phenomenon is obtained. These data can now be used to apply the two formulations of aerodynamic sound derived in Section 2.

3.2. Application of formulation A

3.2.1. Integration method

Curle's formulation (8) gives the pressure for an observation point situated in the acoustic field as the sum in 2-D of a surface and a line integral:

$$\hat{p}_V(\mathbf{x},\omega) = -\rho_\infty \iint_V \widehat{u_i u_j}\,\frac{\partial^2 \hat{G}_0}{\partial y_i \partial y_j}\,\mathrm{d}\mathbf{y} \tag{19}$$

and

$$\hat{p}_\Sigma(\mathbf{x},\omega) = -\int_\Sigma \hat{p}\,\frac{\partial \hat{G}_0}{\partial y_i}\,n_i\,\mathrm{d}\Sigma(\mathbf{y}). \tag{20}$$

The convection and refraction effects by the mean flow are neglected as usual in Lighthill's analogy. These effects are weak for the low Mach number considered ($M = 0.12$), and can be taken into account by the use of a convected wave equation. The Doppler effect is described for example in the study by Inoue and Hatakeyama [32].

The first step is the storage of the aerodynamic quantities during two periods of the CFD simulation, that is to say $73\Delta t$. The velocity components, needed for Eq. (19), are recorded on the whole computational domain. The line pressure appearing in Eq. (20) is recorded on the 350 grid points of the cylinder circumference. The ambient properties are those used in the aerodynamic computation, namely $c_\infty = 340\,\mathrm{m/s}$ and $\rho_\infty = 1.225\,\mathrm{kg/m^3}$. Second, the source terms $u_i u_j$ and p are transformed into the frequency domain using the Fourier transform defined by Eq. (3). The spatial derivatives are applied on the Green function, by using analytical formulae (given in Appendix A.1). The integration is then carried out for the eleven first frequencies and for each point of an acoustic meshgrid, which is a polar grid with 101 grid points radially and 72 grid points in the θ direction. It extends from $r_x = 0$ to about $r_x = 100D$. For the surface integration on the unstructured mesh, a Gauss method of the third order is employed, and the line integral is evaluated with the trapezoidal rule. Lastly, an inverse Fourier transform is used to recover the acoustic signal in the time domain.

3.2.2. Results

The solution of Curle's analogy is plotted in Fig. 5(a) and (b), which, respectively, represent the pressure obtained by the surface integral on the whole computational domain and the line integral on the cylinder boundary. The integral over the flowfield is the most difficult to evaluate and is generally not calculated, with the exception of Cox et al. [31], who show a directivity but no validation was provided. Fig. 5(a) depicts a lateral quadrupole field at frequency f_0, and with level 10 times lower than the crossflow dipole-like field of Fig. 5(b). These results are expected since the dipole contribution is of order $M^{5/2}$ whereas the quadrupole term is of order $M^{7/2}$. Moreover, the origin of the radiation for the surface integral is not the centre of the cylinder, but is at about $x_1/D = 1 - 2$ behind.

The total sound field is then dominated by the crossflow dipole with a frequency equal to the shedding cycle frequency f_0, corresponding to the period of fluctuation of the lift coefficient. The transverse component of the dipole can be separated from its longitudinal component, as shown, respectively, in Fig. 6(a) and (b). This separation is somehow artificial but allows to distinguish the contribution of the drag and lift forces. Fig. 6(a) depicts a dipole field with a direction at right

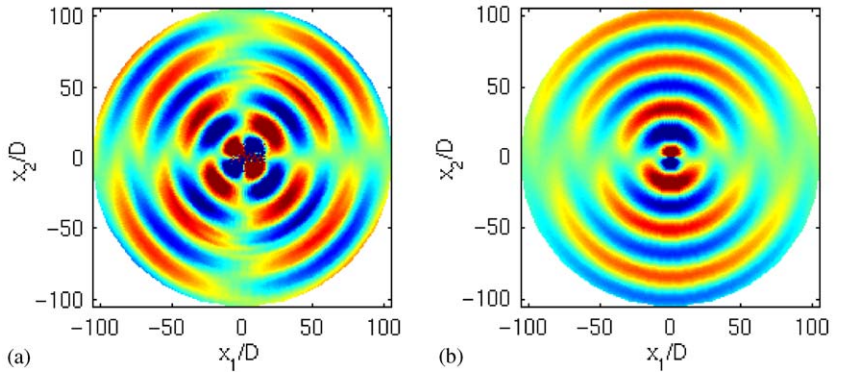

Fig. 5. Acoustic pressure predicted by the Curle analogy: (a) contribution of the surface integral (19) (levels of pressure between -0.5 and $+0.5\,\mathrm{Pa}$); (b) contribution of the line integral (20) (levels of pressure between -5 and $+5\,\mathrm{Pa}$).

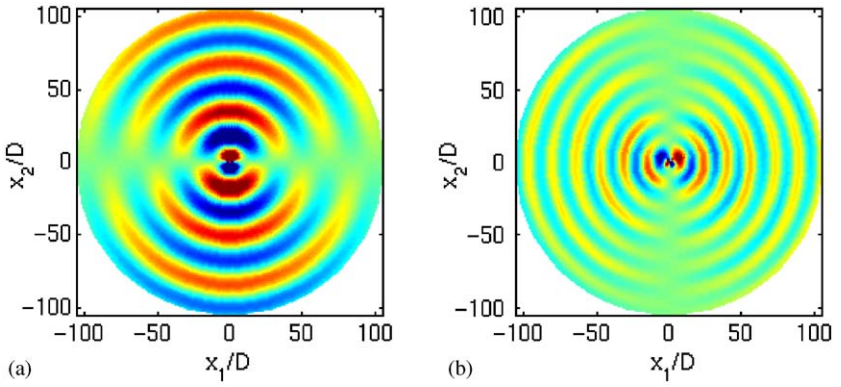

Fig. 6. (a) Acoustic pressure obtained by integrating the x_2-component of the surface pressure (levels are between -5 and $+5$ Pa). (b) Acoustic pressure obtained by integrating the x_1-component of the surface pressure (levels are between -0.5 and $+0.5$ Pa).

angles to the flow direction, and a frequency equal to the shedding cycle frequency f_0. The dipole in Fig. 6(b) is parallel to the direction of the flow, and the sound frequency is doubled. The acoustic level of the longitudinal contribution is about 5% of that of the transverse contribution. The radiation in the streamwise direction is essentially due to the longitudinal component, while the global directivity is pronounced in the direction perpendicular to the flow, largely dominated by the transverse component at the fundamental frequency f_0. These results are similar to those obtained by Cox et al. [31], or more recently by Inoue and Hatakeyama [32].

3.3. Application of formulation B

3.3.1. Numerical implementation

With the use of the tailored Green function (18), only the knowledge of velocity components is required. The general formulation (9) can be split in a direct and a scattered part:

$$\hat{p}_0(\mathbf{x},\omega) = -\rho_\infty \iint_V \widehat{u_i u_j} \frac{\partial^2 \hat{G}_0}{\partial y_i \partial y_j} \, \mathrm{d}\mathbf{y}, \tag{21}$$

and

$$\hat{p}_s(\mathbf{x},\omega) = -\rho_\infty \iint_V \widehat{u_i u_j} \frac{\partial^2 \hat{G}_s}{\partial y_i \partial y_j} \, \mathrm{d}\mathbf{y}, \tag{22}$$

where $\hat{G}_0$ is the free-field Green function in cylindrical coordinates (12), and $\hat{G}_s$ the scattering part defined by Eq. (17). The integration procedure is identical to that used in the previous section, and the second derivatives of the tailored Green function are given in Appendix A.2. The $m = 12$ first terms of the sum in Eq. (9) are sufficient to obtain a good estimation of the tailored Green function.

3.3.2. Results and comparisons

Fig. 7(a) and (b) represent the pressure field obtained by using the direct and scattered parts of the tailored Green function. The similarities with the results of the Curle method in Fig. 5(a) and (b) are underlined in Fig. 8. The profiles of the pressure radiated in free-field (without the cylinder) are in very good agreement for the two angles plotted in Fig. 8(a). This agreement was expected since the only difference for this part between the formulations A and B is the coordinate system in which the free-field Green function is expressed. The profiles in Fig. 8(b), corresponding to the pressure field induced by the cylinder surface are also consistent. The signals are perfectly in phase, but the results of the Curle analogy are about 10% higher than those from the formulation using the tailored Green function. This difference in amplitude is difficult to interpret, and only some conjectures can be made. First, when the domain for the surface integration has been chosen, the influence of the location of the domain boundaries was noticed. The whole CFD domain has therefore been retained, but a truncature effect may still be present. It would affect all the surface integrals (the T_{ij} integration of the Curle method, and the two parts of the formulation based on the tailored Green function). Another explanation may be associated with the accuracy of the evaluation of the surface pressure in the CFD code. The eventual errors would then affect the line integration of Curle's method. As suggested by a referee, the fact that no account is taken of viscous stresses can explain a part of the observed difference, even if the explicit integration of viscous terms generally lead to a negligible influence to the radiated noise. Nevertheless, despite this small discrepancy, the equivalence of both methods is clearly disclosed in Fig. 9, where the directivity of the far-field sound at $64D$ is plotted.

From a numerical point of view, the Curle method is obviously advantageous insofar as the surface effects are represented by a line integral in 2-D reducing by one dimension the integration to be solved. It is interesting to note that, in the analytical developments of Section 2, no assumption has been made concerning the compactness of the surface. The two formulations are therefore valid in all configurations with either compact or non-compact surfaces in the flow.

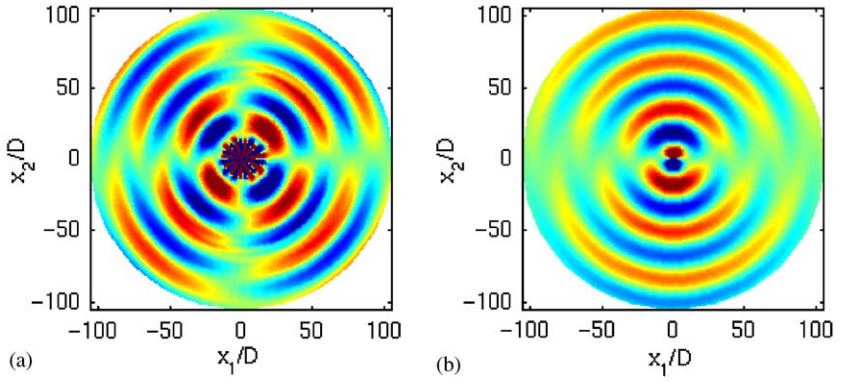

Fig. 7. Acoustic pressure predicted with the tailored Green function: (a) contribution of the free-field part (21) (levels of pressure between −0.5 and +0.5 Pa); (b) contribution of the scattered part (22) (levels of pressure between −5 and +5 Pa).

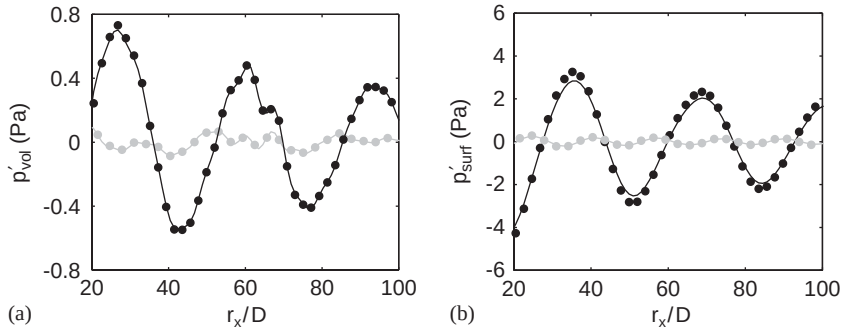

Fig. 8. (a) Profiles of the incident pressure field in the radial direction: (——) direct part of the tailored Green function at $\theta = 45°$; (• • •) surface integral part of the Curle method at $\theta = 45°$; (——) direct part of the tailored Green function at $\theta = 90°$; (• • •) surface integral part of the Curle method at $\theta = 90°$. (b) Profiles of the pressure induced by the surface in the radial direction: (——) scattered part of the tailored Green function at $\theta = 90°$; (• • •) line integral part of the Curle method at $\theta = 90°$; (——) scattered part of the tailored Green function at $\theta = 0°$; (• • •) line integral part of the Curle method at $\theta = 0°$.

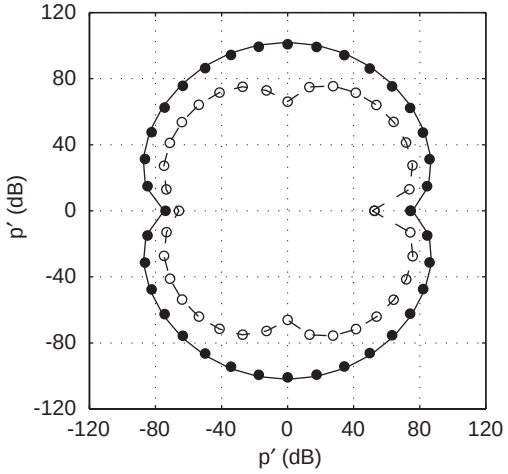

Fig. 9. Overall sound pressure level directivity patterns at $r_x = 64D$: (– – –), surface integral part of the Curle method; (——), line integral part of the Curle method; (• • •), direct part of the tailored Green function; (○ ○ ○), scattered part of the tailored Green function.

3.3.3. The nature of cylinder noise sources

Since the integral over the aerodynamic sources is of quadrupole type and is negligible, this is the scattered sound field from the cylinder that is heard even if the acoustic energy comes from the vorticity itself. Howe [11] suggests that the principal event is the sudden acceleration of the vorticity as it leaves the cylinder influence. The vortices grow in strength until they are released into the flow and rapidly accelerate to the convection velocity at the end of the formation region. The deformation and/or the acceleration of the vorticity should occur at the frequency f_0 and may be related to the interactions of two counter-rotating vortices as they encounter together after the

formation length. Further investigation is required to define more precisely the particular vortical event generating the near-field energy.

The principal feature ignored by the 2-D approach is the fully 3-D turbulent state of the wake. The consequence on the acoustic field would be a finite axial correlation length whereas this length is infinite in the present acoustic calculations. In practice, this will not affect the previous analysis since the axial coherence length is of the order of the diameter D for a turbulent wake, so that each correlated element of the wake near the cylinder can be assumed to be acoustically compact. Besides, no attempt is made in this paper to predict the additional turbulent broadband noise.

4. Description of the diffraction

4.1. A modelling of the diffraction by a cylinder

In order to give further insight into the physical process giving rise to the enhancement of the flow noise, a simple modelling of the diffraction by a cylinder is proposed. Assuming that vorticity is compact, the quadrupoles originating from the unsteady flow are in phase and are equivalent to a point quadrupole. This modelling is a purely formal one and may need very careful interpretation if ambiguous results are to be avoided. The artificial acoustic quadrupole used for the illustration of the diffraction problem is only an equivalent source. A similar analysis has been conducted by Davies [14] who considered multipole point sources near a sphere.

The quadrupole can be obtained by adding up four simple sources, two identical positive sources at $(a+L+l/2, l/2)$ and at $(a+L-l/2, -l/2)$ and two negative sources at $(a+L+l/2, -l/2)$ and at $(a+L-l/2, l/2)$, with the same strength, the origin of the Cartesian coordinates being the centre of the cylinder of radius a. L is the distance between the end of the cylinder and the centre of the four sources group, and l denotes the separation between the simple sources. The notations are summarized in Fig. 10. The frequency of the sources is that calculated in Section 3, $f_0 = 274\,\text{Hz}$. Their strength is scaled to match the amplitude of the quadrupole field obtained from the T_{ij} contribution with the free-field Green function. The diffraction of the quadrupole field is computed by adding the scattered pressure of the four individual sources, as defined by Eq. (15). A value $l = 0.5\,\text{mm}$ for the separation between the sources ensures $kl = 2.5 \times 10^{-2} \ll 1$, so that the quadrupole is compact. The distance L between the quadrupole and the

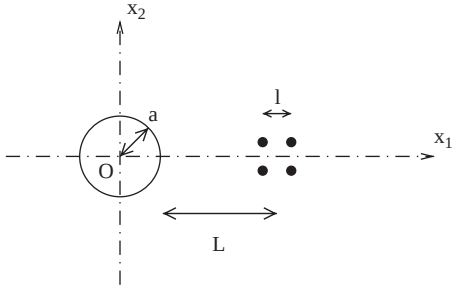

Fig. 10. Notations used for the definition of the quadrupole source.

cylinder is varied until the scattered amplitude reaches that of the scattered field obtained numerically by integrating the T_{ij} with the scattering part of the tailored Green function G_s.

4.2. Pressure field in the vicinity of the cylinder

The results for $L = 1.4$ cm are presented in Figs. 11 and 12. The quadrupole radiation in Fig. 11(a) agrees well with that of Figs. 5(a) or 7(a), except that the sound is harmonic and the small effect of the higher frequencies is not represented. In particular, the radiated field associated with the drag fluctuations at $2f_0$ (see Fig. 6(b)) cannot be reproduced. The scattered field in Fig. 11(b) is of dipole type with axis perpendicular to the stream direction, confirming that the diffraction of a single lateral quadrupole by a cylinder is a crossflow dipole. The amplitude of the pressure fluctuations is compared with that obtained from the formulation based on the tailored

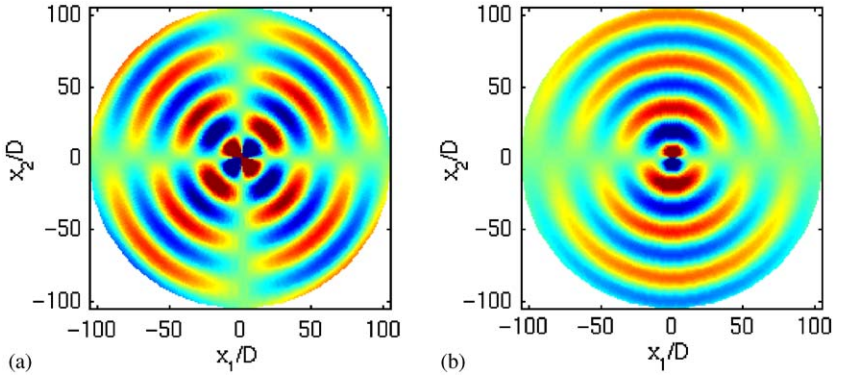

Fig. 11. (a) Acoustic pressure radiated by the single lateral quadrupole (levels are between −0.5 and +0.5 Pa). (b) Acoustic pressure scattered from the cylinder (levels are between −5 and +5 Pa).

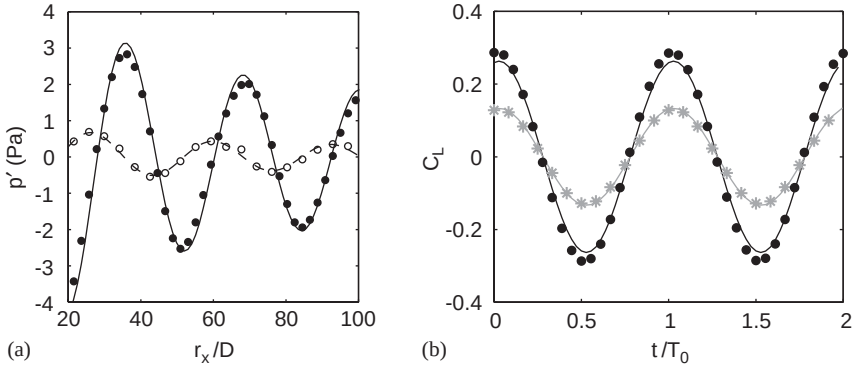

Fig. 12. (a) Pressure profiles in the radial direction for $\theta_x = 90°$, obtained by: (− − −) direct field from the lateral quadrupole, (○ ○ ○) direct field from aerodynamic sources T_{ij} with the free-field Green function G_0, (——) scattered field of the single quadrupole by the cylinder, (● ● ●) scattered field of the T_{ij} with the Green function G_s. (b) Fluctuating lift coefficient obtained by: (——), scattering of the equivalent quadrupole by the cylinder; (✳ ✳ ✳) direct field from the quadrupole; (——), total field (scattered + direct); (● ● ●), CFD simulation of Section 3.

Green function in Fig. 12(a). Remembering that the amplitude, the frequency of the quadrupole, and the distance L have been adjusted, the directivity and the amplitude of the scattered pressure agree fairly well with that computed in Section 3.

The pressure at the cylinder surface is investigated by plotting the contributions of the direct and scattered fields to the pressure at the cylinder wall in Fig. 12(b). The two contributions are equal since the rigid condition $\partial p/\partial n = 0$ implies a perfect reflection of the incident pressure at the wall. When the two contributions are added to obtain the total field (13), the amplitude and phase of the fluctuating pressure are in reasonably good agreement with the computed results of Section 3, dominated by the oscillations of the lift force.

The pressure in the vicinity of the wall is not an acoustic one since it occurs within a wavelength of the radiated sound. In this region, the propagation factor $\exp(\mathrm{i}kr)$ is almost constant, and the motion is essentially incompressible ($k \to 0$). The Helmholtz equation formally reduces to Laplace's equation in the limit of very low wavenumber, and, as a first approximation, it is typical that the corresponding static problem ($k = 0$) has to be solved. The conversion process of near-field energy into far-field energy is the same whether the pressure originates from an artificial quadrupole source or from the flow itself. The pressure is directly related to the velocity field by a Poisson's equation. The amplification process generating æolian tones is thus determined by the aerodynamic pressure in the vicinity of the cylinder, responding immediately to any vorticity change. The extent to which this increase of sound energy is effected depends crucially upon the boundary condition associated with the scattering body ($\partial p/\partial n = 0$ for a rigid surface), and upon its shape. This is illustrated by varying two parameters, namely the distance L and the radius a of the cylinder.

4.3. Influence of the parameters

Since the exact Green function (18) is valid for both compact and non compact cylinders, the parameters characteristic of the model can be varied in order to recover the classical diffraction properties in the short- and long-wavelength limits.

For this 2-D case, the acoustic power is estimated on a circle of radius $r_{x_0} = 64D = 2.44\,\mathrm{m}$, enclosing the source:

$$P = \oint \overline{(p - p_\infty)\mathbf{u} \cdot \mathbf{n}}\,\mathrm{d}S \simeq \frac{r_{x_0}}{\rho_\infty c_\infty} \int_0^{2\pi} \overline{(p - p_\infty)^2}\,\mathrm{d}\theta_x$$

for locally plane waves. The overline denotes the time average over one shedding period. P_d designates the power of the direct field, that of the quadrupole alone, and P_s is the scattered power from the cylinder.

First, the influence of the distance between the cylinder and the quadrupole source is depicted in Fig. 13(a). The surface and the source are both compact ($ka \ll 1$ and $kl \ll 1$ respectively). For $kL < 0.3$, the power is enhanced by the diffraction process. The configuration chosen to match the numerical results of Section 3, is marked by an asterisk, and corresponds to an increase of 18 dB. When the quadrupole is not close to the cylinder on the wavelength scale, the surface radiates a genuine dipole field but the scattered power is negligible compared with the power of the incident field from the quadrupole. This illustrates the fact that the acoustic power delivered by the source is determined by conditions within a wavelength [17,10]. If the cylinder is compact, a very much

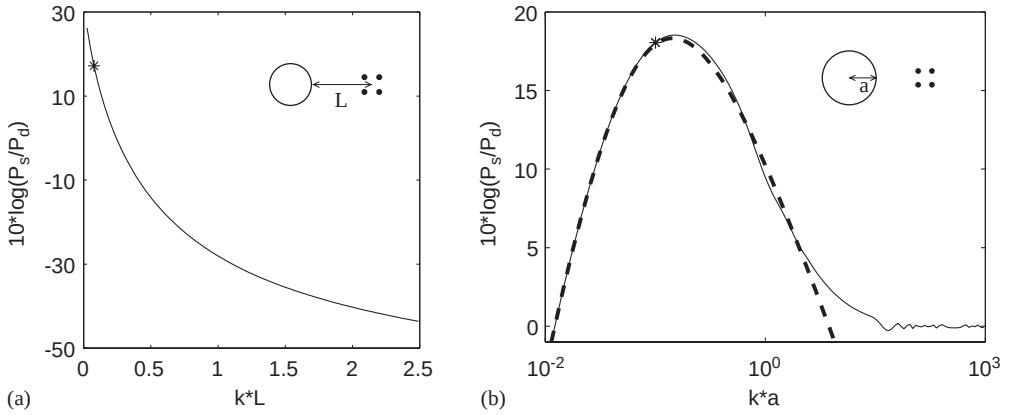

Fig. 13. Evolution of the difference of the acoustic power in dB induced by the diffraction as a function of the distance L between the cylinder and the quadrupole (a) ($a = 1.9$ cm); the radius a of the cylinder (b) ($L = 1.4$ cm, i.e. $kL \simeq 0.07$), obtained from the numerical result (——), and from the asymptotic form Eq. (B.1) (– – –).

larger dipole field is radiated. Coming back to the æolian tone problem, the influence of L corresponds to the effect of varying the formation length L_f for a fixed frequency. In a control perspective, a lengthening of the formation region will therefore reduce the diffraction enhancement.

Finally, the radius a of the cylinder is varied. The evolution curve of Fig. 13(b) indicates a well-defined maximum for the scattered power, which is very close to the value chosen for the comparison with Section 3 (marked by an asterisk). In the long-wavelength limit ($ka \ll 1$), as shown by the limiting values derived in Appendix B, little is scattered and this is scattered in a dipole-like pattern with the radiation direction perpendicular to the x_1-axis. When the radius is large relative to the wavelength (typically $ka > 2\pi$), the dependence of the scattered power on the observation angle becomes more and more complex. The approximation of geometrical acoustics then applies. Reflection doubles the radiation on the source side, and there is a shadow zone behind the cylinder. The total power radiated remains the same, being merely redistributed in the different directions.

5. Conclusion

Curle's formulation shows how the sound radiated by a flow past a cylinder may be associated to the unsteady pressure force on the body, resulting in a dipole-like acoustic source. The construction of a tailored Green's function, satisfying the boundary condition $\partial p/\partial n = 0$, indicates that Curle's dipoles are not physical sources but only equivalent sources modelling the diffraction of the quadrupole sound. This is illustrated numerically by comparing the two formulations with the unsteady flow from an incompressible simulation as input. The diffraction process, occurring within a wavelength of the radiated sound, is responsible for the enhancement of the flow noise by converting near-field energy into the form of acoustic waves. As in the simple acoustic modelling presented in the last section, the near-field pressure is primarily aerodynamic.

In the æolian tone problem, the only physical sound source is the flow itself, and this source is closely linked to a particular vortical event in the near wake, just after the formation region.

Acknowledgements

The authors would like to thank PSA Peugeot Citroën for their financial support of part of this research.

Appendix A. Derivatives of the Green functions

A.1. Derivatives of the 2-D free-field Green function in frequency domain

A.1.1. First derivatives

$$\frac{\partial \hat{G}_0(\mathbf{x}|\mathbf{y},\omega)}{\partial y_i} = \frac{k}{4\mathrm{i}}\,\frac{r_i}{r}\,H_1^{(1)}(kr), \quad \text{where } r_i = |x_i - y_i|. \tag{A.1}$$

A.1.2. Second derivatives

$$\frac{\partial^2 \hat{G}_0(\mathbf{x}|\mathbf{y},\omega)}{\partial y_i \partial y_j} = \frac{1}{4\mathrm{i}}\left\{-k^2\,\frac{r_i r_j}{r^2}\,H_0^{(1)}(kr) + k\left(\frac{2r_i r_j}{r^3} - \frac{\delta_{ij}}{r}\right)H_1^{(1)}(kr)\right\}. \tag{A.2}$$

A.2. Derivatives of the tailored Green function

The second derivatives of Eq. (18) are:

$$\begin{aligned}\frac{\partial^2 \hat{G}_1(\mathbf{x}|\mathbf{y},\omega)}{\partial y_i \partial y_j} = \frac{1}{4\mathrm{i}}\sum_{m=0}^{+\infty} \varepsilon_m H_m^{(1)}(kr_x) \times \Bigg\{ & -m\left(\sin(m\phi)\,\frac{\partial^2\theta_y}{\partial y_i \partial y_j} + m\cos(m\phi)\,\frac{\partial\theta_y}{\partial y_i}\,\frac{\partial\theta_y}{\partial y_j}\right)A_m \\ & - mk\sin(m\phi)\left(\frac{y_j}{r_y}\,\frac{\partial\theta_y}{\partial y_i} + \frac{y_i}{r_y}\,\frac{\partial\theta_y}{\partial y_j}\right)B_m \\ & + k\cos(m\phi)\left[\left(\frac{\delta_{ij}}{r_y} - \frac{y_i y_j}{r_y^3}\right)B_m + k\,\frac{y_i y_j}{r_y^2}\,C_m\right]\Bigg\},\end{aligned} \tag{A.3}$$

where $\phi = \theta_y - \theta_x$, $A_m = A_m^0 + A_m^s$, $B_m = B_m^0 + B_m^s$, $C_m = C_m^0 + C_m^s$, with:

$$A_m^0 = J_m(kr_y),$$

$$A_m^s = -\alpha_m H_m^{(1)}(kr_y),$$

$$B_m^0 = -J_{m+1}(kr_y) + \frac{m}{kr_y}\,J_m(kr_y),$$

$$B_m^s = \alpha_m \left[H_{m+1}^{(1)}(kr_y) - \frac{m}{kr_y} H_m^{(1)}(kr_y) \right],$$

$$C_m^0 = J_{m+2}(kr_y) - \frac{m+1}{kr_y} J_{m+1}(kr_y) - \frac{m}{kr_y} \left[J_{m+1}(kr_y) - \frac{m}{kr_y} J_m(kr_y) \right],$$

$$C_m^s = \alpha_m \left\{ -H_{m+2}^{(1)}(kr_y) + \frac{m+1}{kr_y} H_{m+1}^{(1)}(kr_y) + \frac{m}{kr_y} \left[H_{m+1}^{(1)}(kr_y) - \frac{m}{kr_y} H_m^{(1)}(kr_y) \right] \right\},$$

$$\alpha_m = \frac{J_{m-1}(ka) - J_{m+1}(ka)}{H_{m-1}^{(1)}(ka) - H_{m+1}^{(1)}(ka)} = \frac{kaJ_{m+1}(ka) - mJ_m(ka)}{kaH_{m+1}^{(1)}(ka) - mH_m^{(1)}(ka)},$$

$$\frac{\partial \theta_y}{\partial y_1} = -\frac{y_2}{r_y^2}, \quad \frac{\partial \theta_y}{\partial y_2} = \frac{y_1}{r_y^2}, \quad \frac{\partial^2 \theta_y}{\partial y_1^2} = \frac{2y_1 y_2}{r_y^4}, \quad \frac{\partial^2 \theta_y}{\partial y_2^2} = -\frac{2y_1 y_2}{r_y^4}, \quad \frac{\partial^2 \theta_y}{\partial y_1 \partial y_2} = \frac{y_2^2 - y_1^2}{r_y^4}.$$

The factors with superscript 0 define the free-field part of the tailored Green function, and the superscript s denotes the scattered part of the tailored Green function.

Appendix B. Scattering of a lateral quadripole by a cylinder—Long-wavelength limit

B.1. Direct field

The pressure field at an observer $\mathbf{x}$ from an incident lateral quadripole ($i = 1$, $j = 2$ in Eq. (A.2)) of amplitude A at $\mathbf{y}$ can be expressed as

$$\hat{p}_d = \frac{A}{4\mathrm{i}} \left(-k^2 \frac{r_1 r_2}{r^2} H_0^{(1)}(kr) + k \frac{2r_1 r_2}{r^3} H_1^{(1)}(kr) \right).$$

With the assumption of a distant sound field ($|\mathbf{x}| = r_x \gg |\mathbf{y}| = r_y$), the second term is neglected, and the asymptotic form of the Hankel function is used to get:

$$\hat{p}_d \simeq \frac{\mathrm{i}Ak^2}{4} \frac{x_1 x_2}{r_x^2} \sqrt{\frac{2}{\pi k r_x}} \mathrm{e}^{\mathrm{i}(kr_x - \pi/4)} = \frac{\mathrm{i}Ak^2}{4} \cos(\theta_x) \sin(\theta_x) \sqrt{\frac{2}{\pi k r_x}} \mathrm{e}^{\mathrm{i}(kr_x - \pi/4)}.$$

The intensity of the incident field is then:

$$I_d(\mathbf{x}) = K|\hat{p}_d|^2 = K \frac{A^2 k^3}{8\pi r_x} \cos^2(\theta_x) \sin^2(\theta_x),$$

where $K = 1/(2\rho_\infty c_\infty)$, and the radiated power can be estimated as

$$P_d(\mathbf{x}) = \int_0^{2\pi} I_d(r_x, \theta_x) r_x \, \mathrm{d}\theta_x = K \frac{A^2 k^3}{32}.$$

B.2. Scattered field

The scattered wave of the lateral quadripole by a cylinder of radius a, located at the origin of the coordinate system, is deduced from Eq. (A.3). The polar coordinates of the quadripole centre are $(r_y, 0)$, so that the expression is simplified:

$$\hat{p}_s(\mathbf{x},\omega) = \frac{A}{4\mathrm{i}} \sum_{m=0}^{+\infty} \varepsilon_m m \sin(m\theta_x) H_m^{(1)}(kr_x) \frac{J_{m-1}(ka) - J_{m+1}(ka)}{H_{m-1}^{(1)}(ka) - H_{m+1}^{(1)}(ka)} \times \left[-\frac{1}{r_y^2} H_m^{(1)}(kr_y) - \frac{k}{r_y} H_{m+1}^{(1)}(kr_y) + \frac{m}{r_y^2} H_m^{(1)}(kr_y) \right].$$

The asymptotic form of the Hankel functions for r_x very large is used:

$$H_m^{(1)}(kr_x) \simeq \sqrt{\frac{2}{\pi k r_x}} \mathrm{e}^{\mathrm{i}kr_x - (1/2)\mathrm{i}\pi(m+1/2)}.$$

Expressing both Bessel and Hankel functions in terms of their amplitude and phase angles, defined by

$$J_m(z) = C_m(z) \sin[\delta_m(z)] \quad \text{and} \quad H_m^{(1)}(z) = -\mathrm{i} C_m(z) \mathrm{e}^{\mathrm{i}\delta_m(z)},$$

it yields [18]:

$$\frac{J_{m-1}(z) - J_{m+1}(z)}{H_{m-1}^{(1)}(z) - H_{m+1}^{(1)}(z)} = \frac{\dfrac{\mathrm{d}}{\mathrm{d}z} J_m(z)}{\dfrac{\mathrm{d}}{\mathrm{d}z} H_m^{(1)}(z)} = \frac{-C_m'(z) \sin[\delta_m'(z)]}{\mathrm{i} C_m'(z) \mathrm{e}^{\mathrm{i}\delta_m'(z)}} = \mathrm{i}\mathrm{e}^{-\mathrm{i}\delta_m'(z)} \sin[\delta_m'(z)].$$

Finally, the scattered field is written as

$$\hat{p}_s(\mathbf{x},\omega) = \frac{A}{2r_y^2} \sqrt{\frac{2}{\pi k r_x}} \mathrm{e}^{\mathrm{i}kr_x} \sum_{m=1}^{+\infty} m \sin(m\theta_x) \mathrm{e}^{-\mathrm{i}\delta_m'(ka) - (1/2)\mathrm{i}\pi(m+1/2)} \sin[\delta_m'(ka)] \times \left[\frac{m-1}{r_y^2} H_m^{(1)}(kr_y) - \frac{k}{r_y} H_{m+1}^{(1)}(kr_y) \right],$$

and the scattered power is estimated as

$$P_s(\mathbf{x}) = K \int_0^{2\pi} |\hat{p}_s(\mathbf{x},\omega)|^2 r_x \, \mathrm{d}\theta_x = K \frac{A^2}{2kr_y^2} \sum_{m=1}^{+\infty} m^2 \sin^2[\delta_m'(ka)] \left| \frac{m-1}{r_y} H_m^{(1)}(kr_y) - kH_{m+1}^{(1)}(kr_y) \right|^2.$$

In the long-wavelength limit, $ka \ll 1$, values for the derivative of the phase angles δ_m' are given by the following approximate formulas [18]:

$$\delta_m'(ka) \simeq -\frac{\pi m}{(m!)^2} \left(\frac{ka}{2} \right)^{2m} \quad (m > 0),$$

so that, for $ka \ll 1$, only the cylindrical wave corresponding to $m = 1$ is important in the scattered wave, because $|\delta_1'| \gg |\delta_2'|, |\delta_3'|, \ldots$.

The asymptotic behaviour for the Hankel function $H_m^{(1)}(kr_y) = J_m(kr_y) + \mathrm{i}\mathrm{N}_m(kr_y)$ is deduced from:

$$J_m(kr_y) \simeq \frac{1}{m!}\left(\frac{kr_y}{2}\right)^m \quad \text{and} \quad \mathrm{N}_m(kr_y) \simeq -\frac{(m-1)!}{\pi}\left(\frac{2}{kr_y}\right)^m \quad (kr_y \ll 1, m > 0).$$

Taking $\sin(\delta_m') \sim \delta_m'$, the ratio of the acoustic power, $Q = P_s/P_d$, for $m = 1$ reads:

$$Q(\mathbf{x}) \simeq \frac{16}{k^4 r_y^2}[\delta_1'(ka)]^2 k^2 [N_2(kr_y)]^2 \simeq \frac{16(ka)^4}{(kr_y)^6}. \tag{B.1}$$

This expression is similar to that found by Crighton [10] with a different approach of the diffraction problem. Q becomes very small for $k \longrightarrow 0$. Moreover, noting that I_d has an angular dependence proportional to $\cos^2(\theta_x)\sin^2(\theta_x)$, the direct field is a lateral quadrupole. Similarly, $I_s \sim \sin^2(\theta_x)$, so that the scattered field is a dipole with a directivity perpendicular to the x_1-direction. For $ka \ll 1$, *little is scattered, and this is scattered in a dipole-like pattern*, as shown in Fig. 13(b).

References

[1] N. Curle, The influence of solid boundaries upon aerodynamic sound, *Proceedings of the Royal Society of London A* 231 (1955) 505–514.

[2] E.Y. Yudin, On the vortex sound of rotating rods, Technical Memorandum No. 1136, NACA, 1947, *Zhurnal Tekhnicheskoi Fiziki (Trans.)* 14 (9) (1944) 561.

[3] O.M. Phillips, The intensity of æolian tones, *Journal of Fluid Mechanics* 1 (1956) 607–624.

[4] M.E. Goldstein, Effect of solid boundaries, in: *Aeroacoustics*, McGraw-Hill, New York, 1976, pp. 145–153 (Chapter 3).

[5] W.K. Blake, Dipole sound from cylinders, in: *Mechanics of Flow-Induced Sound and Vibration*, *vol. 1: General Concepts and Elementary Sources*, Academic Press, Inc., New York, 1986, pp. 219–287 (Chapter 4).

[6] A. Powell, Theory of vortex sound, *Journal of the Acoustical Society of America* 36 (1964) 177–195.

[7] J.E. Ffowcs Williams, Hydrodynamic noise, *Annual Reviews—Fluid Mechanics* 1 (1969) 197–222.

[8] J.E. Ffowcs Williams, L.H. Hall, Aerodynamic sound generation by turbulent flow in the vicinity of a scattering half-plane, *Journal of Fluid Mechanics* 40 (1970) 657–670.

[9] D.G. Crighton, F.G. Leppington, On the scattering of aerodynamic noise, *Journal of Fluid Mechanics* 46 (3) (1971) 577–597.

[10] D.G. Crighton, Basic principles of aerodynamic sound generation, *Progress in Aerospace Sciences* 16 (1) (1975) 31–96.

[11] M.S. Howe, Sound generation in a fluid with rigid boundaries, *Acoustics of Fluid–Structures Interactions*, Cambridge University Press, Cambridge, 1998, pp. 164–166 (Chapter 3).

[12] A.P. Dowling, Vortex sound, in: D.G. Crighton, A.P. Dowling, J.E. Ffowcs Williams, M. Heckl, F.G. Leppington (Eds.), *Modern Methods in Analytical Acoustics*: *Lectures Notes*, Springer, London, 1992, pp. 355–377.

[13] J.C. Hardin, S.L. Lamkin, Aeroacoustic computation of cylinder wake flow, *AIAA Journal* 22 (1) (1984) 51–57.

[14] H.G. Davies, The radiated fields of multipole point sources near a solid spherical surface, *Journal of Fluid Mechanics* 43 (3) (1970) 597–606.

[15] D.G. Crighton, Acoustics as a branch of fluid mechanics, *Journal of Fluid Mechanics* 106 (1981) 261–298.

[16] M.J. Lighthill, On sound generated aerodynamically I. General theory, *Proceedings of the Royal Society of London A* 211 (1952) 564–587.
[17] P.E. Doak, Acoustic radiation from a turbulent fluid containing foreign bodies, *Proceedings of the Royal Society of London A* 254 (1960) 129–145.
[18] P.M. Morse, K.U. Ingard, *Theoretical Acoustics*, McGraw-Hill, New York, 1968.
[19] P.J. Morris, The scattering of sound from a spatially distributed axisymmetric cylindrical source by a circular cylinder, *Journal of the Acoustical Society of America* 97 (5) (1995) 2651–2656.
[20] A. Powell, Aerodynamic noise and the plane boundary, *Journal of the Acoustical Society of America* 32 (8) (1960) 982–990.
[21] D.S. Jones, Aerodynamic sound due to a source near a half-plane, *Journal of the Institute of Mathematics and its Applications* 9 (1972) 114–122.
[22] M.S. Howe, Contributions to the theory of aerodynamic sound, with application to excess noise and the theory of the flute, *Journal of Fluid Mechanics* 71 (1975) 625–673.
[23] C.H.K. Williamson, Vortex dynamics in the cylinder wake, *Annual Reviews—Fluid Mechanics* 28 (1996) 477–539.
[24] J.P. Batham, Pressure distributions on circular cylinders at critical Reynolds number, *Journal of Fluid Mechanics* 57 (1973) 209–228.
[25] E. Achenbach, E. Heinecke, On vortex shedding from smooth and rough cylinders in the range of Reynolds numbers 6×10^3 to 5×10^6, *Journal of Fluid Mechanics* 109 (1981) 239–251.
[26] A. Roshko, Experiments on the flow past a circular cylinder at very high Reynolds number, *Journal of Fluid Mechanics* 10 (1961) 345–356.
[27] J.D. Revell, R.A. Prydz, A.P. Hays, Experimental study of aerodynamic noise vs drag relationships for circular cylinders, *AIAA Journal* 16 (9) (1978) 889–897.
[28] E. Achenbach, Distribution of local pressure and skin friction around a circular cylinder in cross-flow up to $\mathrm{Re} = 5 \times 10^6$, *Journal of Fluid Mechanics* 34 (1968) 625–639.
[29] C. Cantwell, D. Coles, An experimental study of entrainment and transport in the turbulent near wake of a circular cylinder, *Journal of Fluid Mechanics* 136 (1983) 321–374.
[30] S. Kumarasamy, R. Korpus, J.B. Barlow, Computation of noise due to flow over a circular cylinder, *Second Computational Aeroacoustics Workshop on Benchmark Problems*, NASA CP-3352, 1997, pp. 297–304.
[31] J.S. Cox, K.S. Brentner, C.L. Rumsey, Computation of vortex shedding and radiated sound for a circular cylinder: subcritical to transcritical Reynolds numbers, *Theoretical and Computational Fluid Dynamics* 12 (1998) 233–253.
[32] O. Inoue, N. Hatakeyama, Sound generation by a two-dimensional circular cylinder in a uniform flow, *Journal of Fluid Mechanics* 471 (2002) 285–314.